International Journal of Bifurcation and Chaos, Vol. 25, No. 9 (2015) 1550117 (18 pages)

DOI: 10.1142/S0218127415501175

Numerical Study of Periodic Traveling Wave Solutions for the Predator–Prey Model with Landscape Features

Ana Yun
Department of Mathematics, Korea University, Seoul 136-713, Republic of Korea

Jaemin Shin
Institute of Mathematical Sciences, Ewha W. University, Seoul 120-750, Republic of Korea

Yibao Li
School of Mathematics and Statistics, Xi'an Jiaotong University, Xi'an 710049, P. R. China

Seunggyu Lee and Junseok Kim*
Department of Mathematics, Korea University, Seoul 136-713, Republic of Korea
**cfdkim@korea.ac.kr*

Received September 5, 2014; Revised March 2, 2015

We numerically investigate periodic traveling wave solutions for a diffusive predator–prey system with landscape features. The landscape features are modeled through the homogeneous Dirichlet boundary condition which is imposed at the edge of the obstacle domain. To effectively treat the Dirichlet boundary condition, we employ a robust and accurate numerical technique by using a boundary control function. We also propose a robust algorithm for calculating the numerical periodicity of the traveling wave solution. In numerical experiments, we show that periodic traveling waves which move out and away from the obstacle are effectively generated. We explain the formation of the traveling waves by comparing the wavelengths. The spatial asynchrony has been shown in quantitative detail for various obstacles. Furthermore, we apply our numerical technique to the complicated real landscape features.

Keywords: Dirichlet boundary; periodic traveling waves; predator–prey model; landscape features; numerical periodicity.

1. Introduction

The spatial behavior of species has been considered as a central problem in the ecological field [Cross & Hohenberg, 1993]. For the interactions of species, predator and prey equations have been mathematically studied after Lotka's [Lotka, 1925] and Volterra's [Volterra, 1926] models. These studies are usually considered on the homogeneous domain. However, the realistic domain is a large-scale domain with heterogeneity [Benson *et al.*, 1993]. In experimental results [Ims & Andreassen, 2000; Lambin *et al.*, 1998; Mackin-Rogalska & Nabaglo,

*Author for correspondence

1990; MacKinnon *et al.*, 2001; Myberget, 1973; Ranta & Kaitala, 1997; Steen *et al.*, 1996], predator and prey densities often show the periodic traveling wave on a large domain. From the mathematical point of view, the spatiotemporal movement has been studied for the predator–prey system moving out from the obstacle which constructs periodic traveling solutions [Deng *et al.*, 2013; Li & Qiao, 2012; Sheratt & Smith, 2008; Smith *et al.*, 2008; Upadhyay *et al.*, 2010]. For the first time, Sherratt *et al.* modeled the landscape features by applying the homogeneous Dirichlet boundary at the edge of the obstacles [Sherratt *et al.*, 2002].

To solve the reaction–diffusion equations, numerical schemes such as an implicit–explicit scheme [Ascher *et al.*, 1995; Garvie, 2007; Ruuth, 1995] and a theta method [Borzi, 2004] have been developed. These numerical methods are generally calculated on the homogeneous domain and the numerical study on the nonhomogeneous domain has been generally restricted to the whole domain [Crooks *et al.*, 2004]. Therefore, it is worthwhile to study robust numerical methods to have numerical solutions on the realistic domain. By the numerical experiments, theoretical results can be supported [Borzi, 2004; Crooks *et al.*, 2004; Wang, 2012; Waite *et al.*, 2014].

In this paper, we investigate the periodic traveling wave solutions with complicated landscape features. We present a numerical method by using a boundary control function [Li *et al.*, 2013] to accurately treat the boundary of obstacle. Moreover, we propose an accurate algorithm to calculate the numerical periodicity. By employing the numerical periodicity algorithm, we have efficient numerical solutions without extra calculations. An operator splitting method is used where a linear diffusion term is solved by using multigrid method and a nonlinear term is solved by using the fourth-order Runge–Kutta method [Zhong, 1996]. We investigate the mechanism of the periodic traveling wave solutions for the predator–prey model with landscape features through numerical experiments.

This paper is organized as follows. The governing system is briefly introduced in Sec. 2. We describe the numerical scheme in Sec. 3 including the algorithm for the periodic numerical traveling wave solution. Moreover, the numerical scheme with the Dirichlet boundary is presented. In Sec. 4, various numerical results are obtained. Discussions are included in Sec. 5.

2. The Governing System

The governing system for the ratio-dependent predator–prey model having prey-dependent functional response [Sherratt *et al.*, 2002; Banerjee & Banerjee, 2012] with the diffusion is:

$$\frac{\partial U}{\partial t} = rU\left(1 - \frac{U}{U_0}\right) - \frac{ckUV}{1+kU} + D_1\Delta U, \tag{1}$$

$$\frac{\partial V}{\partial t} = -bV + \frac{akUV}{1+kU} + D_2\Delta V, \tag{2}$$

where $U(\mathbf{x},t)$ and $V(\mathbf{x},t)$ are the population densities of prey and predators, respectively. Δ is the Laplacian operator. D_1, D_2 are prey and predator diffusion coefficients, respectively. Here r is a growth factor of the prey, b is a death rate of the predator in the absence of the prey, U_0 is the maximal carrying capacity of the prey, a and c are interactions between the prey and the predator, and k measures the satiation effect [Dunbar, 1986]. By introducing dimensionless variables

$$\tilde{t} = rt, \quad \tilde{u} = \frac{U}{U_0}, \quad \tilde{v} = \frac{cV}{rU_0}, \quad \tilde{\mathbf{x}} = \frac{\mathbf{x}}{\sqrt{\frac{D_1}{r}}},$$

$$\tilde{\alpha} = \frac{a}{b}, \quad \tilde{\beta} = \frac{r}{a}, \quad \tilde{\gamma} = kU_0, \quad \tilde{\sigma} = \frac{D_2}{D_1},$$

we have the nondimensional system after omitting tilde notation:

$$u_t = u(1-u) - \frac{\gamma uv}{1+\gamma u} + \Delta u, \tag{3}$$

$$v_t = \frac{\gamma uv}{\beta(1+\gamma u)} - \frac{v}{\alpha\beta} + \sigma\Delta v. \tag{4}$$

Here u and v are non-negative. The governing system has the equilibrium points at $(0,0)$, $(1,0)$, and at least one point having positive values $(\overline{u},\overline{v})$ where $\overline{u}$ and $\overline{v}$ are defined as $\overline{u} = 1/(\gamma(\alpha-1))$ and $\overline{v} = (1-\overline{u})(1+\gamma\overline{u})/\gamma$, respectively. For positiveness, $\alpha > 1$. The domain Ω is constituted as $\Omega = \Omega_o \cup \partial\Omega_o \cup \Omega_c \subset \mathbb{R}^d$, $d = 1, 2$, where Ω_o is an obstacle domain, $\partial\Omega_o$ is an obstacle boundary, and Ω_c is a physical domain as shown in Fig. 1. The boundary condition, $\partial\Omega$, is imposed as the no-flux boundary condition:

$$\mathbf{n}\cdot\nabla u = \mathbf{n}\cdot\nabla v = 0, \tag{5}$$

where $\mathbf{n}$ is the unit vector normal to the domain boundary $\partial\Omega$. Moreover, the homogeneous Dirichlet

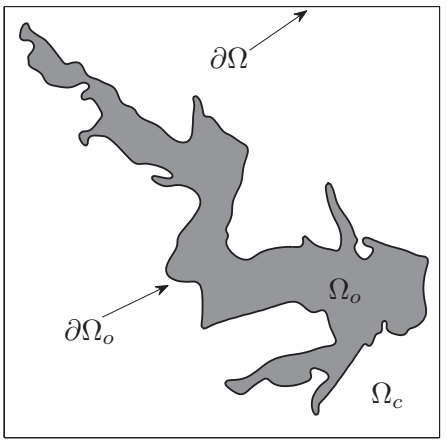

Fig. 1. Neumann boundary condition for the domain boundary $\partial\Omega$ and the homogeneous Dirichlet boundary condition for the obstacle domain boundary $\partial\Omega_o$.

boundary condition is assumed for the obstacle domain $\partial\Omega_o$ which means both the predator and prey die at the obstacle boundary.

3. Numerical Solution

In this section, we present a robust numerical scheme for the discretized governing system and an accurate algorithm for calculating numerical periodicity is proposed. The governing systems (3) and (4) are solved by using an operator splitting method: For the first step, we solve the system of nonlinear ordinary differential equations $u_t = F_1(u, v)$ and $v_t = F_2(u, v)$, where

$$F_1(u, v) := u(1 - u) - \frac{\gamma uv}{1 + \gamma u}, \tag{6}$$

$$F_2(u, v) := \frac{\gamma uv}{\beta(1 + \gamma u)} - \frac{v}{\alpha\beta}. \tag{7}$$

Here, we solve them by using the fourth-order Runge–Kutta method [Zhong, 1996]. The second step is solving the system of diffusion equations $u_t = \Delta u$ and $v_t = \sigma\Delta v$. Here, fully implicit time and centered difference space discretizations are used.

3.1. *Discretization*

Let us discretize the two-dimensional domain $\Omega = (0, L) \times (0, L)$. A uniform spatial step size $h = L/N_x = L/N_y$ for even positive integers N_x and N_y is assumed. We use a temporal step size $\Delta t = T/N_t$ where T is the total time and N_t is a positive integer. The numerical solutions to $u(x, y, t)$ and $v(x, y, t)$ are approximated at cell-centers by $u^n_{ij} \equiv u(x_i, y_j, n\Delta t)$ and $v^n_{ij} \equiv v(x_i, y_j, n\Delta t)$, where $x_i = (i - 0.5)h$ and $y_j = (j - 0.5)h$ for $i = 1, 2, \ldots, N_x$, $j = 1, 2, \ldots, N_y$, and $n = 0, 1, \ldots, N_t$. The zero Neumann boundary conditions are imposed at the domain boundary, $u^n_{0j} = u^n_{1j}$, $u^n_{i0} = u^n_{i1}$, $u^n_{N_x+1,j} = u^n_{N_x j}$, and $u^n_{i,N_y+1} = u^n_{iN_y}$.

We treat the obstacle boundary by introducing the boundary control function G which is defined as

$$G_{ij} = \begin{cases} 0, & \text{if } (x_i, y_j) \in \Omega_o \cup \partial\Omega_o, \\ 1, & \text{otherwise.} \end{cases} \tag{8}$$

Then we denote the discrete physical domain by $\Omega^h_c = \{(x_i, y_j) \,|\, G_{ij} = 1\}$. Figures 2(a) and 2(b) illustrate the domain with the obstacle (shaded region) and the discrete domain with the boundary control function G_{ij}, respectively. If $G_{ij} = 0$, then $u^{n+1}_{ij} = u^*_{ij} = 0$ and $v^{n+1}_{ij} = v^*_{ij} = 0$. Moreover, u_{ij} and v_{ij} with $G_{ij} = 0$ are automatically used on the obstacle including the zero Dirichlet boundary condition at the obstacle boundary.

Then the operator splitting scheme is presented as follows:

Step 1. A system of $u_t = F_1(u, v)$ and $v_t = F_2(u, v)$ is solved by using Runge–Kutta method. Then we have the intermediate variables u^* and v^* with the initial conditions u^n and v^n.

Step 2. To obtain approximations u^{n+1} and v^{n+1}, we solve $u_t = \Delta u$ and $v_t = \sigma\Delta v$ with the initial conditions u^* and v^*. The discretized system is written as:

$$\frac{u^{n+1}_{ij} - u^*_{ij}}{\Delta t} = G_{ij}\Delta_d u^{n+1}_{ij}, \tag{9}$$

$$\frac{v^{n+1}_{ij} - v^*_{ij}}{\Delta t} = \sigma G_{ij}\Delta_d v^{n+1}_{ij}, \tag{10}$$

where the discrete Laplacian for the Cartesian domain is defined as

$$\Delta_d u^{n+1}_{ij} = \frac{u^{n+1}_{i-1,j} + u^{n+1}_{i+1,j} - 4u^{n+1}_{ij} + u^{n+1}_{i,j-1} + u^{n+1}_{i,j+1}}{h^2}.$$

To have efficient numerical solutions for Step 2, we use a multigrid method [Briggs, 1987]. For the multigrid method, detailed description is summarized in [Li *et al.*, 2013]. Note that the dimensional case and the radially symmetric domain can be similarly defined.

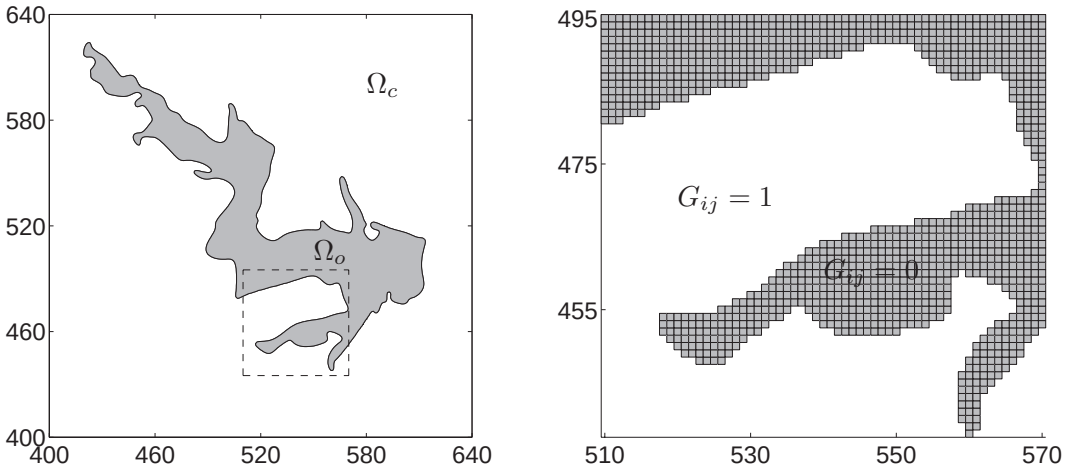

Fig. 2. (a) Description of the domain where the shaded region is the obstacle and (b) closed view of discrete domain with the boundary control function G_{ij}.

3.2. *Algorithm for numerical periodicity*

In this section, we will describe an efficient algorithm to find the periodic traveling wave solution [Zhang *et al.*, 2007] in one-dimensional space. When the numerical solution u_i^n satisfies $u_i^{n+1} = u_{i+p}^n$ for some integers p and i, we call u_i^n is a traveling wave solution. Especially, this solution is space-periodic with period of hp for a space step size h. For some integer τ, if u_i^n satisfies $u_i^{n+\tau} = u_i^n$, the solution u_i^n is time-periodic with period of $\tau\Delta t$ for the time step Δt. Let us define the velocity l as $u_i^{n+1} = u_{i+l}^n$. Then the velocity l/k satisfies $u_i^{n+k} = u_{i+l}^n$.

Definition 3.1. The solution u_i^n satisfying $u_i^{n+k} = u_{i+l}^n$ is called the periodic traveling wave solution [Zhang *et al.*, 2007].

That is, the periodic traveling wave solution is the space and time periodic solution. Then we propose an algorithm on the one-dimensional space to detect the numerical periodicity in the following:

Algorithm 1. The numerical periodicity is obtained by calculating the smallest velocity T_p with following steps:

Step 1. Initial conditions for u and v are given as small random perturbations from the stationary solutions $\overline{u}$ and $\overline{v}$, respectively.

Step 2. Let $u^{n_{\text{ref}}}$ and $v^{n_{\text{ref}}}$ be solutions at the reference time.

The discrete l_2-norm error is defined as

$$e^n = \sqrt{\frac{1}{N_x}\sum_{i=1}^{Nx}((u_i^n - u_i^{n_{\text{ref}}})^2 + (v_i^n - v_i^{n_{\text{ref}}})^2)},$$

for $n > n_{\text{ref}}$.

Step 3. Calculate the local maximum and local minimum errors.

If $e^{m-2} - e^{m-1} < 0$ and $e^{m-1} - e^m > 0$, the temporal error has the local maximum. While $e^{l-2} - e^{l-1} > 0$ and $e^{l-1} - e^l < 0$ where $l > m$, the error has the local minimum. When the error reaches the local minimum and $|e^{n_{\text{ref}}} - e^l| < \text{tol}$, we define the numerical periodicity as $T_p = l - n$. Therefore, we have one-period from n_{ref} to $n_{\text{ref}} + T_p$.

If $e^{n_{\text{ref}}} - e^l > \text{tol}$, return to Step 2.

Step 4. To confirm the obtained numerical periodicity T_p, we calculate the error between $n_{\text{ref}} + T_p$ to $n_{\text{ref}} + 2T_p$.

Figure 3(a) shows the description for the one-period of predator with a space-time plot. Figure 3(b) shows the temporal plot of e with the first one-period Step 3 (marked as circles) and the second one-period Step 4 (solid line) of the traveling wave solution. The result suggests that our method performs well to get the period of predator. Moreover, we can use the algorithm Step 3 to find the one-period of the space traveling wave solution when we analyze the spatial amplitude and wavelength.

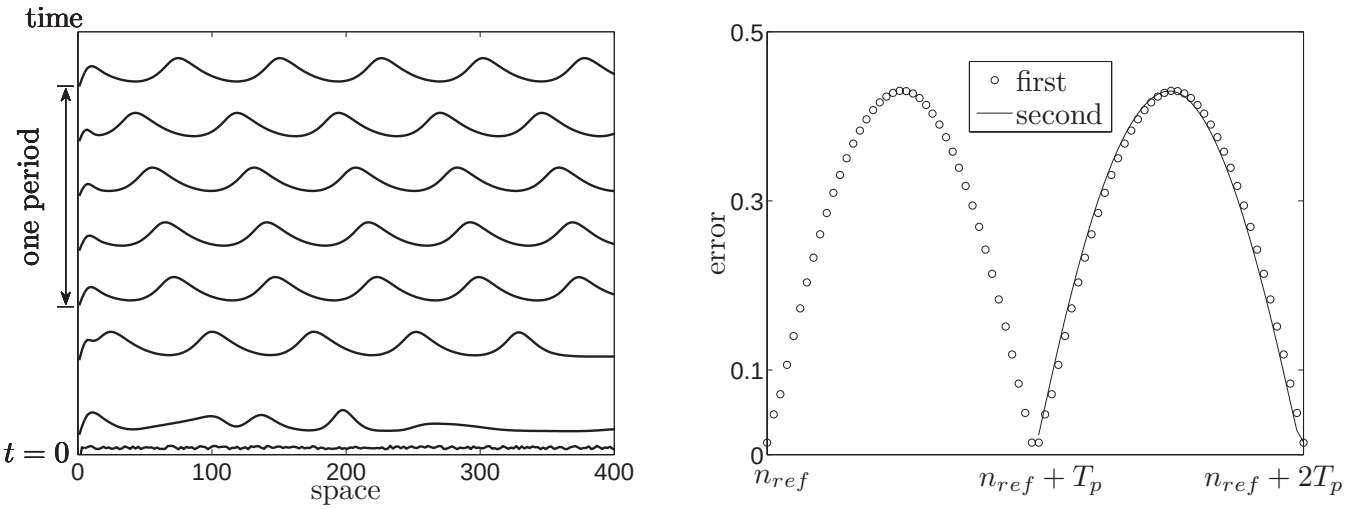

(a) (b)

Fig. 3. (a) A space-time plot for the predator and (b) a temporal plot of e.

4. Numerical Experiments

In this section, we perform various numerical experiments to systematically demonstrate various aspects of the formation of the traveling wave solutions in one-dimensional space, radially symmetric domain, and two-dimensional space. Our numerical experiments confirm the formation of the traveling wave solution in a complicated two-dimensional space. Moreover, the existence of the traveling wave solution and the convergence test are included. In numerical tests, following the field experiments, nondimensionalized values $\alpha = 1.8, \beta = 1.2, \gamma = 4.9$ [Sherratt *et al.*, 2002] are used, unless otherwise specified. The diffusion effect is governed as $\sigma = 2.5$. Unless otherwise specified, we use a tol $= 0.001$, a temporal step size $\Delta t = 0.5$ and a spatial step size $h = 1$. In two-dimensional space, we set initial conditions $u(x, y, 0) = v(x, y, 0) = 0$ in the domain Ω_o and $u(x, y, 0) = 1.1\overline{u} + 0.05\,\mathrm{rand}(x, y)$ and $v(x, y, 0) = 1.1\overline{v} + 0.05\,\mathrm{rand}(x, y)$ in domain Ω_c. Here, $\mathrm{rand}(x, y) \in [-1, 1]$ is a random generated number.

4.1. *Existence of traveling wave solution*

When the kinetic system has a stable limit cycle, there exists traveling wave solution [Kopell & Howard, 1973]. In the kinetic system, the prey and predator systems have complex eigenvalues with given parameter values. After some calculation, the equilibrium solution $(\overline{u}, \overline{v})$ is an unstable node when $\gamma > (\alpha + 1)/(\alpha - 1)$ and the kinetic system shows oscillatory behavior [Sherratt *et al.*, 2002]. To examine the existence of the traveling wave solution numerically, we illustrate the phase portraits with velocity fields (arrows) for the prey and predator in the kinetic system (without diffusion terms). Figure 4 shows two phase portraits arising from different initial points with given parameter sets, i.e. $(u, v) = (\overline{u} + 0.05, \overline{v})$ (marked as a star) and $(u, v) = (\overline{u} + 0.7, \overline{v})$ (marked as a circle) where the square marker represents $(\overline{u}, \overline{v})$ and the solid line

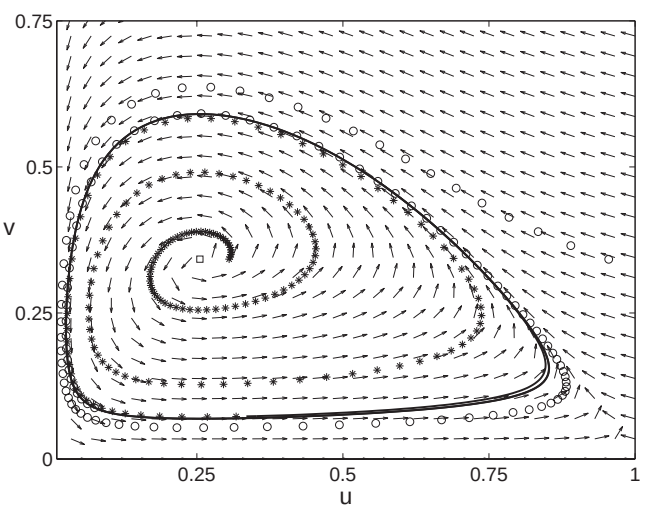

Fig. 4. Phase portraits starting from two points $(u, v) = (\overline{u} + 0.05, \overline{v})$ (marked as a star) and $(u, v) = (\overline{u} + 0.7, \overline{v})$ (marked as a circle) associated with velocity fields (arrows). Here, the square marker represents $(\overline{u}, \overline{v})$ and the solid line represents the stable limit cycle.

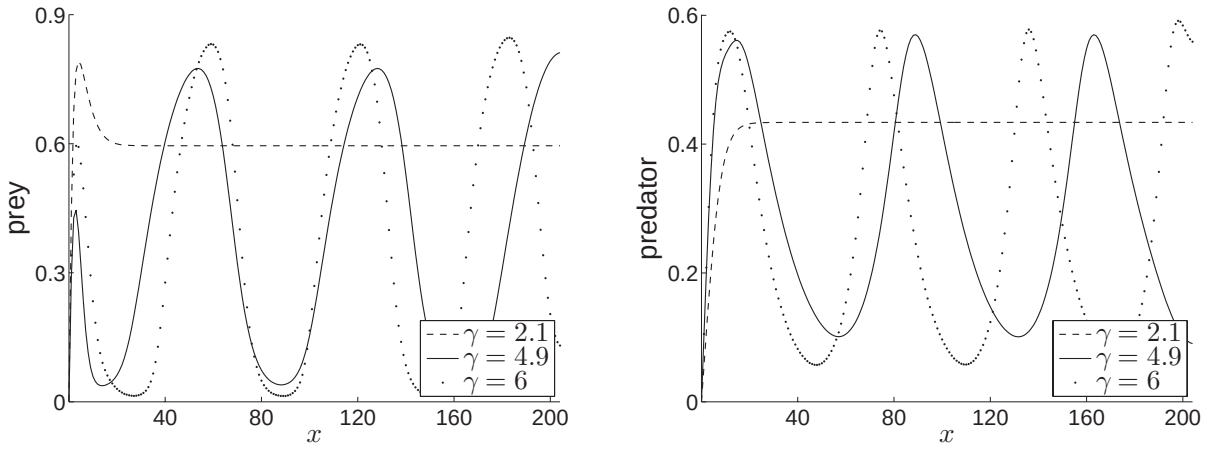

(a) (b)

Fig. 5. (a) Prey solutions and (b) predator solutions with different values of $\gamma = 2.1$, 4.9, and 6.

represents the stable limit cycle. Here, $\Delta t = 0.1$ and $T = 50$ are used for the computation. The temporal evolutions of the phase portraits converge to the limit cycle with two different initial conditions. Hence, the limit cycle is stable and the traveling wave solution for the system exists.

4.2. *Parameter studies*

We calculate the formation of traveling wave solutions having an obstacle with varying parameter values. It is sufficient to show in one-dimensional space. The given parameter set $\alpha = 1.8$, $\beta = 1.2$, and $\gamma = 4.9$ shows oscillatory behavior in the kinetic system, as described in Sec. 4.1. With obstacle at $x = 0$, numerical solutions are obtained with $h = 0.1$ on the domain $(0, 204)$. We terminate the numerical calculation when the solution shows periodicity (see Sec. 3.2). First, we consider different values of $\gamma = 2.1$, 4.9, and 6 [Sherratt *et al.*, 2002]. As shown in Fig. 5, the kinetic solution is stable, if $\gamma = 2.1 < (\alpha + 1)/(\alpha - 1)$, and the kinetic solution shows oscillatory behavior, when γ is larger than $(\alpha + 1)/(\alpha - 1)$. Furthermore, when the governing system is stable, it does not generate traveling wave solution in spite of the presence of obstacle. When the system has a limit cycle, it generates traveling wave solution with obstacle.

Then we consider the effect of β. As a and r are positive in governing systems (1) and (2), β is positive. Here we numerically examine different values of $\beta = 0.4$, 1.2, and 2 as shown in Fig. 6. When the

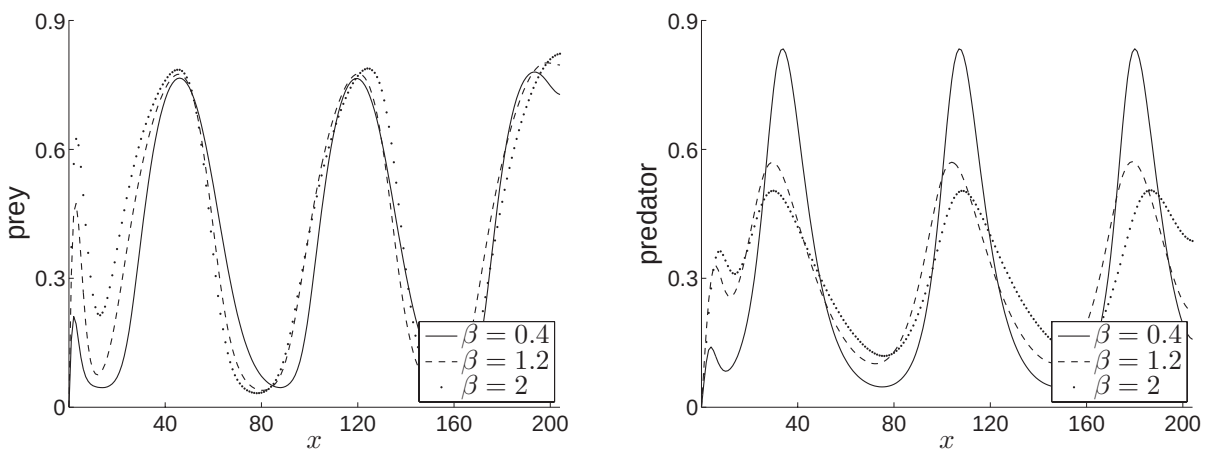

(a) (b)

Fig. 6. (a) Prey solutions and (b) predator solutions with different values of $\beta = 0.4$, 1.2, and 2.

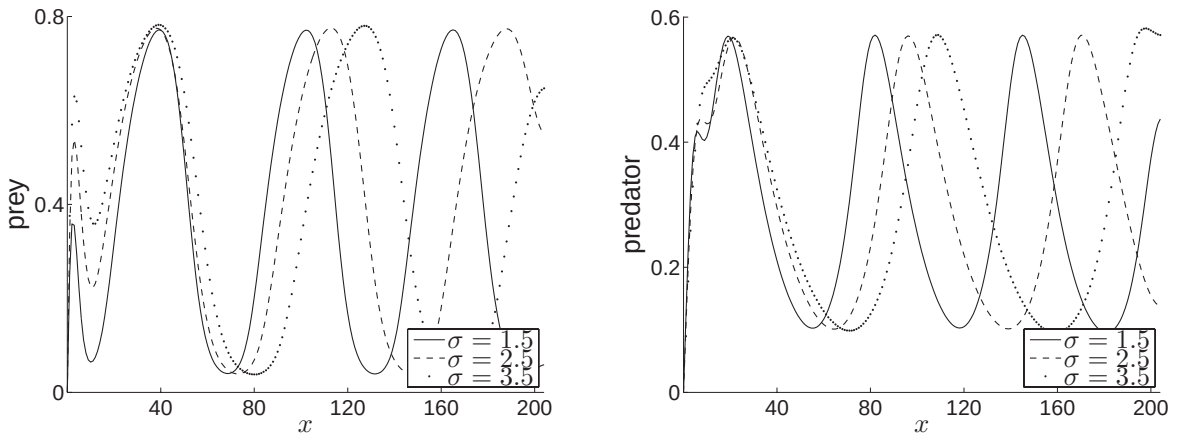

(a) (b)

Fig. 7. (a) Prey solutions and (b) predator solutions with different values of $\sigma = 1.5$, 2.5, and 3.5.

values of β increases, the amplitude of prey solution gets bigger and the amplitude of predator solution gets smaller.

Finally, we consider the effect of σ, which is the ratio of diffusion coefficient, with different values of $\sigma = 1.5$, 2.5, and 3.5. Observing the results in Fig. 7, we can find that as the values of σ are increasing, the wavelength of the numerical solutions gets larger.

4.3. *Convergence test*

We perform numerical calculations to obtain the spatial convergence rate with increasingly finer grids $h = 1/2^{n-8}$ for $n = 8$, 9, 10, and 11 on the one-dimensional domain $(0, 256)$. The initial conditions are given as

$$u(x,0) = \alpha \sin\left(\frac{\pi x}{256}\right) \quad \text{and}$$

$$v(x,0) = \beta \sin\left(\frac{\pi x}{256}\right).$$

Numerical solutions are computed up to time $T = 250$ with a small time step size $\Delta t = h^2$. Since no analytical solutions are available, we use the relative error. We define the error as the discrete l_2-norm of the difference between the grid and the average of the neighboring solutions as follows:

$$e_i^h := u_i^h - \frac{u_{2i-1}^{\frac{h}{2}} + u_{2i}^{\frac{h}{2}}}{2}.$$

The rate of convergence is defined as the ratio of successive errors: $\log_2(\|e^h\|_2/\|e^{\frac{h}{2}}\|_2)$. The obtained errors and rates of convergence using these definitions are given in Table 1. For u and v, the second-order accuracy with respect to the space is observed as expected from the discretization.

Table 1. Error and convergence results with various mesh grids.

Case	256–512	Rate	512–1024	Rate	1024–2048
u: l_2-error	$5.623e{-3}$	2.15	$1.264e{-3}$	2.02	$3.110e{-4}$
v: l_2-error	$1.238e{-3}$	2.03	$3.025e{-4}$	1.93	$7.939e{-5}$

To obtain the convergence rate for the temporal discretization, we fix the spatial grid as 512 and choose a set of decreasing time steps $\Delta t = 1$, 0.5, 0.25, and 0.125. We also run the computation up to time $T = 250$. Note that we define the temporal discrete l_2-norm error as $e_i^{\Delta t} := u_i^{\Delta t} - u_i^{\frac{\Delta t}{2}}$. The obtained errors and rates of convergence are given in Table 2. For both u and v, the first-order accuracy with respect to the time is observed.

4.4. *Numerical solutions in one-dimensional domain*

We examine numerical solutions with an obstacle given at $x = 0$ in the one-dimensional space. The numerical solutions are calculated on the domain $(0, 512)$ with the spatial step size $h = 2$ and temporal step size $\Delta t = 0.5$. The initial conditions are

Table 2. Error and convergence results with various time steps.

Case	1–0.5	Rate	0.5–0.25	Rate	0.25–0.12
u: l_2-error	$1.718e{-3}$	1.05	$8.301e{-4}$	1.02	$4.090e{-4}$
v: l_2-error	$3.981e{-4}$	0.99	$2.005e{-4}$	1.00	$9.995e{-5}$

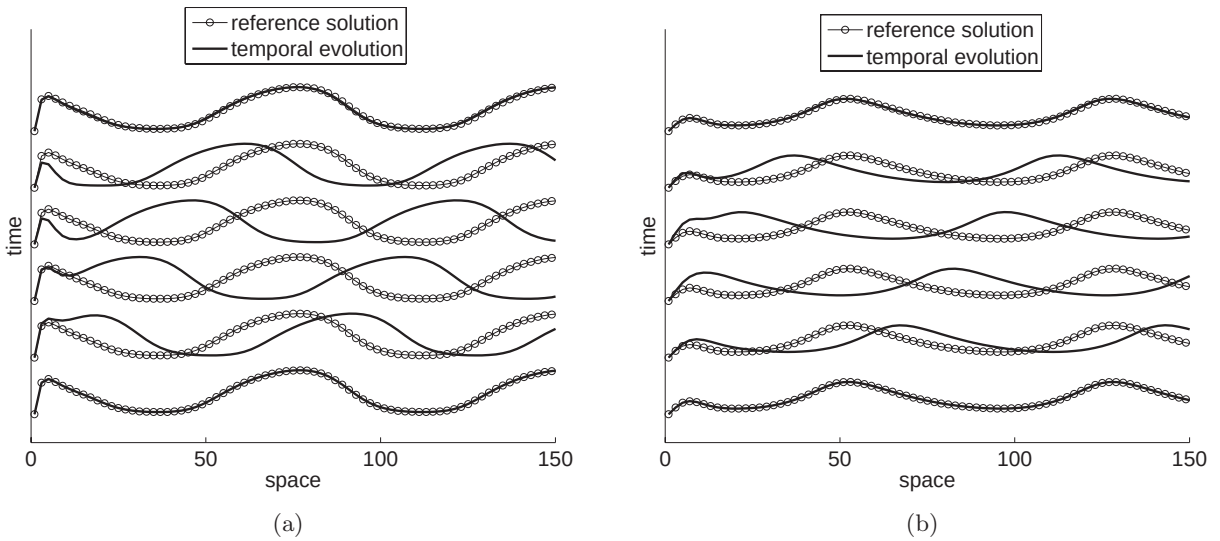

Fig. 8. Space-time plots of the one-period of the periodic traveling wave solutions of (a) the prey and (b) the predator with the obstacle at $x = 0$.

given with two different randomly perturbed values with magnitudes of 0.01 from $(\overline{u}, \overline{v})$. The numerical solution is calculated until it shows periodicity. Figure 8 depicts space-time plots showing a one-period of the periodic traveling wave solutions of the (a) prey and (b) predator (represented as solid lines) overlapped with the reference solutions u^{ref} and v^{ref} (marked as circles), respectively. As the reference solutions are completely overlapped to the temporal evolutions, the periodic traveling waves are obviously observed.

To find the range of the prey and predator during the one-period of the solutions, we show the overlapped space-time plots of u (marked as solid lines) and v (marked as dotted lines) in Fig. 9.

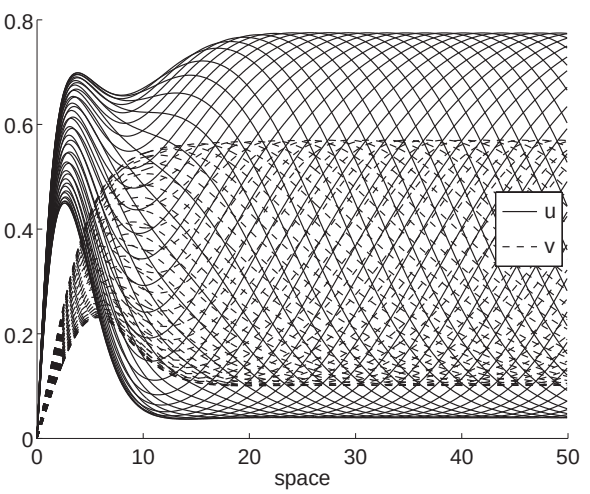

Fig. 9. Space-time plots showing the range of the prey and the predator at the one-period.

In this test, we set the domain as $(0, 163.84)$ with 16 384 spatial grid points. The effect of the Dirichlet boundary to the local region is observed around the zero Dirichlet boundary. In the local region, numerical solutions show one bounded fluctuation for each calculation. The region far from the boundary, the maximum and minimum densities constitute the amplitude of the traveling wave solutions.

4.5. *Numerical solutions in radially symmetric domain*

The governing Eqs. (3) and (4) are rewritten on a radially symmetric domain with respect to r-axis $\Omega = (0, L)$ as follows:

$$u_t = \Delta_r u + u(1-u) - \frac{\gamma uv}{1+\gamma u}, \tag{11}$$

$$v_t = \sigma \Delta_r v + \frac{\gamma uv}{\beta(1+\gamma u)} - \frac{v}{\alpha\beta}. \tag{12}$$

Here, we consider the obstacle size defined as r_b then it is sufficient to calculate the numerical solutions on the domain (r_b, L) [see Fig. 10(a)]. For $h = (L - r_b)/(Nr + 0.5)$, a number of node points N_r, the discretized system for the radially symmetric case is written as:

$$\frac{u_i^{n+1} - u_i^n}{\Delta t} = F_1(u^n, v^n) + G_i \Delta_r u_i^{n+1}, \tag{13}$$

$$\frac{v_i^{n+1} - v_i^n}{\Delta t} = F_2(u^n, v^n) + \sigma G_i \Delta_r v_i^{n+1}, \tag{14}$$

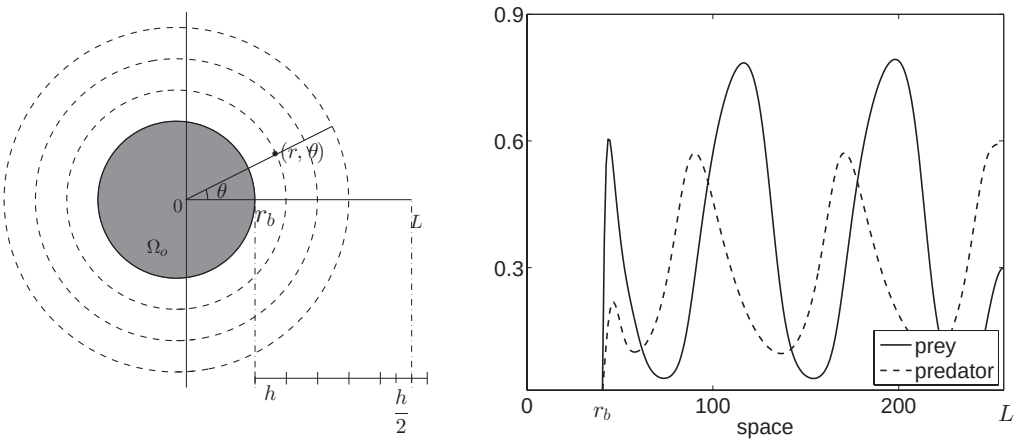

(a) (b)

Fig. 10. (a) Schematic representation of radially symmetric domain and (b) numerical solutions in radially symmetric domain.

for $F_1(u^n, v^n) = u_i^n(1 - u_i^n) - \gamma u_i^n v_i^n/(1 + \gamma u_i^n)$ and $F_2(u^n, v^n) = \gamma u_i^n v_i^n/(\beta(1 + \gamma u_i^n)) - v_i^n/(\alpha\beta)$.

The Laplacian operator in the radially symmetric domain is defined as:

$$\Delta_r u_i^{n+1} = \frac{1}{h^2}\left[\frac{r_{i+\frac{1}{2}}}{r_i}(u_{i+1}^{n+1} - u_i^{n+1}) - \frac{r_{i-\frac{1}{2}}}{r_i}(u_i^{n+1} - u_{i-1}^{n+1})\right],$$

where $r_i = ih$, $r_{i+\frac{1}{2}} = (r_i + r_{i+1})/2$, and $r_{i-\frac{1}{2}} = (r_i + r_{i-1})/2$. We illustrate the numerical result with $r_b = 40$ and $L = 284.5$ for $h = 1$ in Fig. 10(b).

Then we perform numerical calculation to show the effect of the obstacle radius using our scheme following the results in Smith *et al.*'s work [2008]. With varying sizes of an obstacle, the formulation of the traveling wave solution is obtained for an obstacle size r_b. The initial configurations are set as $u(r, 0) = \overline{u} + 0.1\,\mathrm{rand}(r)$, $v(r, 0) = \overline{v} + 0.1\,\mathrm{rand}(r)$ if $r > r_b$ and $u(r_b, 0) = v(r_b, 0) = 0$ otherwise.

In the first test, we calculate amplitudes and wavelengths in radially symmetric domain. The calculations are computed on the domain $(r_b, 512)$ with 2048 mesh grids. The amplitude is defined as half of the average of difference between the maximum and minimum values of each density. Figure 11(a) shows the amplitudes of the prey (marked as circles) and predator (marked as stars) with increasing obstacle sizes r_b, respectively. Likewise, Fig. 11(b) shows the wavelengths of the prey (marked as circles) and predator (marked as stars). The obtained values are drawn with solid lines using a line interpolation and the dashed lines are results obtained

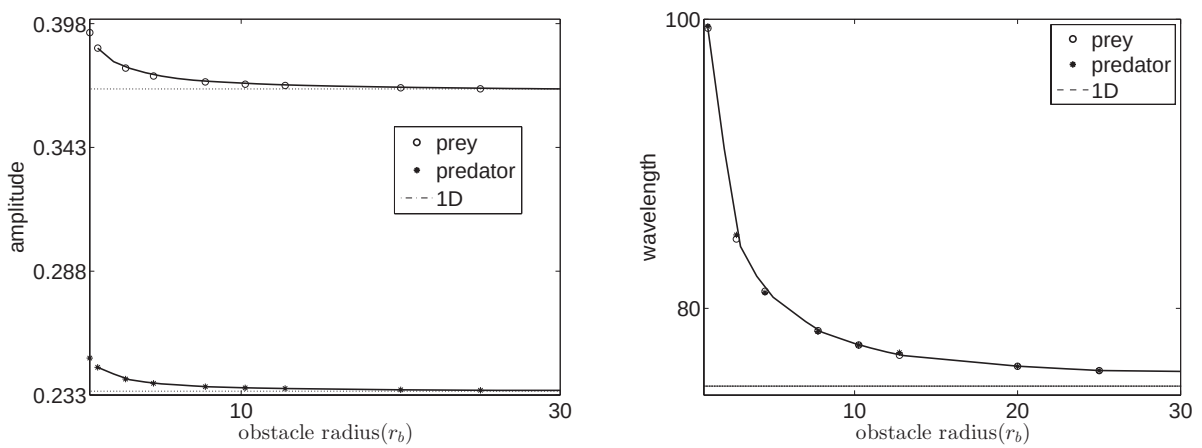

(a) (b)

Fig. 11. Effect of obstacle radius. (a) Amplitudes of the predator with increasing obstacle sizes and (b) wavelengths of the prey and predator.

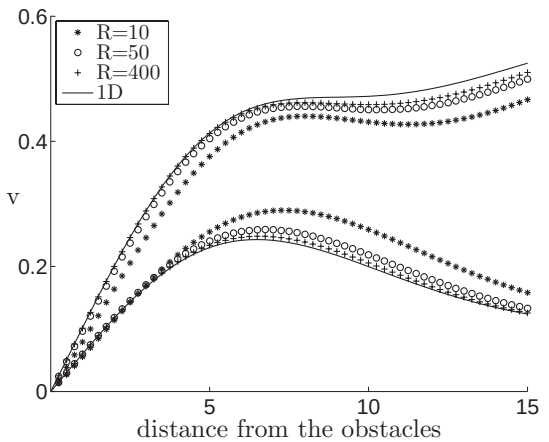

Fig. 12. Range of the predator solution in the local region with increasing obstacle radius.

from the one-dimensional space. These results suggest that the amplitudes decrease as the obstacle radius r_b increases, which approaches dashed lines (results from 1D) for both prey and predator numerical solutions. From Fig. 11(b), we deduce that the formations of the periodic traveling wave solutions have similar pattern between the prey and predator.

Figure 12 shows the convergence of the range of the predator solution with increasing obstacle radius. The star ($r_b = 10$), circle ($r_b = 50$), and plus sign ($r_b = 400$) symbols denote the spatial plots for each obstacle size. Solid lines indicate the maximum (upper side) and the minimum (lower side) of the numerical solution. From these graphs, we attain that the range of increasing obstacle radius converges to the one-dimensional case.

4.6. *Numerical solutions in two-dimensional domain*

The numerical solutions are calculated to show the generation of the wave in the two-dimensional domain. The zero Dirichlet boundary condition at $x = 2$ is imposed on the domain $(0, 128) \times (0, 32)$. In Fig. 13, we display the temporal evolutions of the predator. By the effect of Dirichlet boundary condition, the propagation of waves starting from the left ($x = 2$) generates the traveling wave solution.

For the circular obstacle with a radius of 18, the temporal evolutions of the predator are drawn in Fig. 14. As can seen that the periodic traveling wave solutions around the obstacle are generated. Moreover, as we impose the zero-flux boundary, the waves are orthogonal to the boundary at the edge of the domain boundary.

4.7. *Numerical experiments for convex obstacles*

In this section, we examine some numerical experiments to describe the formation of the periodic traveling wave solutions with convex obstacles.

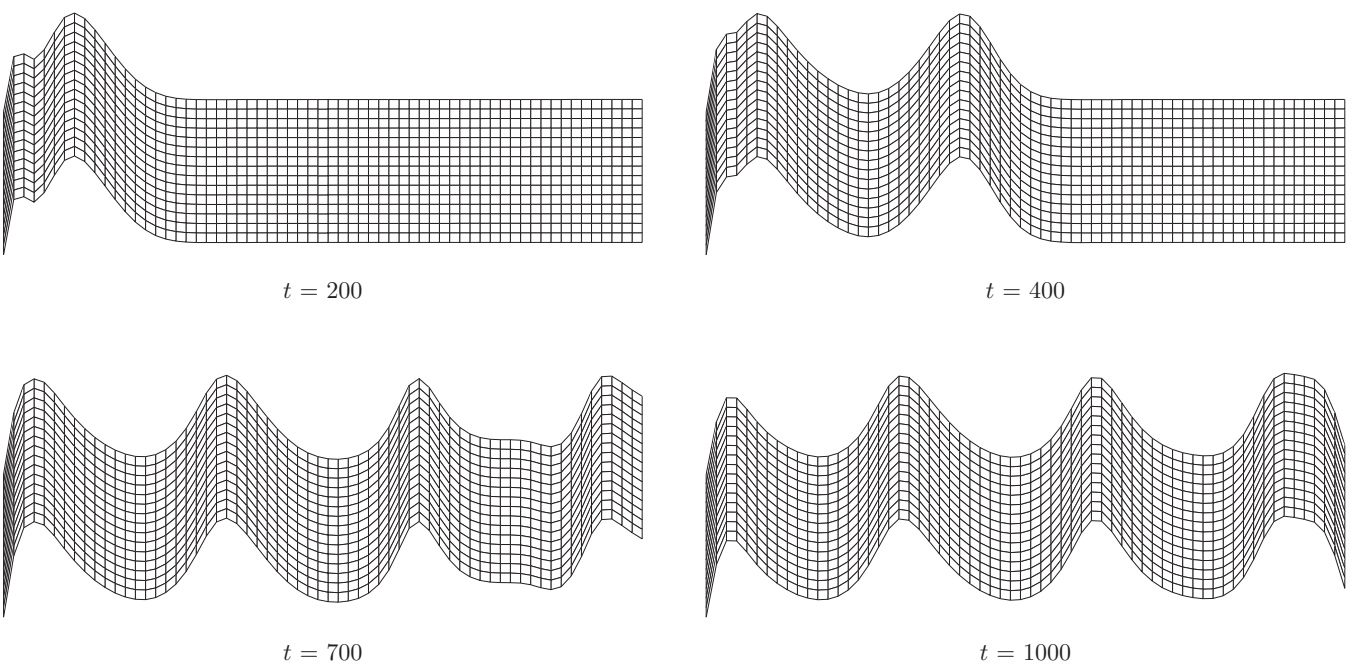

Fig. 13. Temporal evolution of the predator in two-dimensional space with obstacle $(0, 2)$.

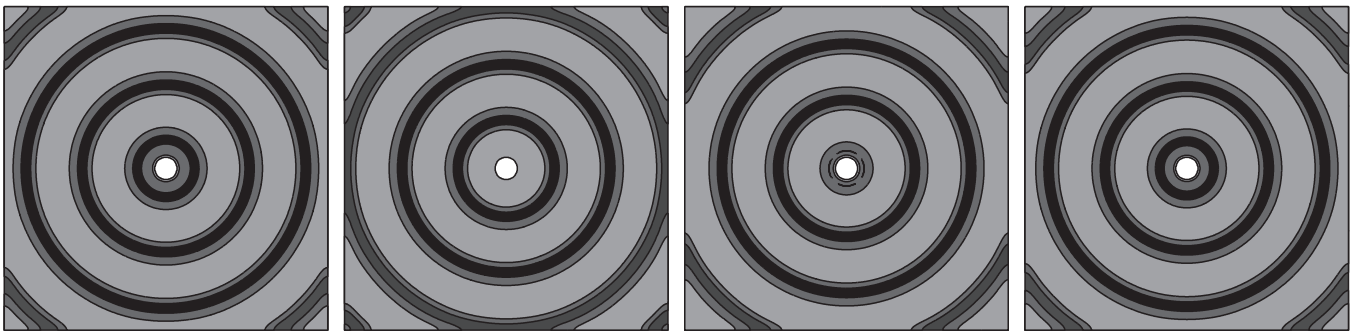

Fig. 14. Temporal evolution with a circular obstacle at $t = 1505$, 1512.5, 1520, and 1525 (from left to right).

4.7.1. *Comparison of circular obstacles*

We compare the radially symmetric domain and 2D with the same obstacle radius. For detailed comparison, Fig. 15(a) is the solution on the radially symmetric domain which is represented in two-dimensional space as shown in Fig. 10(a) (dashed arrow). Here, the obstacle radius $r_b = 25.6$ is imposed. And the predator solution is calculated at time $T = 1420$ on $(r_b, 256.5)$ with a spatial mesh size $h = 1$. Figures 15(a) and 15(b) show the contour plots of the predator solutions obtained from the radially symmetric domain and the two-dimensional space, respectively. Figure 15(c) is the overlapped spatial plots on the radially symmetric and two-dimensional domains. The spatial plots suggest that the generation of traveling wave occurs similarly for all directions surrounding the circle.

4.7.2. *Comparison of rectangular obstacles*

The generation of the traveling wave solutions are observed by rectangular obstacles. On the domain $\Omega = (0, 256) \times (0, 256)$, the obstacle domains $\Omega_o = (0, 10) \times (0, 10)$ (upper row) and $\Omega_o = (0, 50) \times (0, 2)$ (lower row) are considered. The calculations are computed with a spatial mesh size $h = 1$. The contour of the predator solution in the two-dimensional space is overlapped with the stem plot as shown in Fig. 16(a). The x-axis ($x = 1$, marked as circle), axial side ($x = y$, marked as triangle, upper row), and y-axis ($y = 1$, marked as star) are illustrated with stem plots. Figure 16(b) shows overlapped spatial plots at the x-axis ($x = 1$, marked as circle), axial side ($x = y$, marked as triangle, upper row), and y-axis ($y = 1$, marked as star). Observing the results in Fig. 16(b), we can see that the wavelengths are different due to the size of the obstacle. When far from the obstacle, the effect of the obstacle will be much reduced.

4.7.3. *Range of the wavelengths*

The range of the class of wavelengths is examined based on the wavelength. Let us define $w(m)$ as the wavelength of the obstacle for obstacle radius

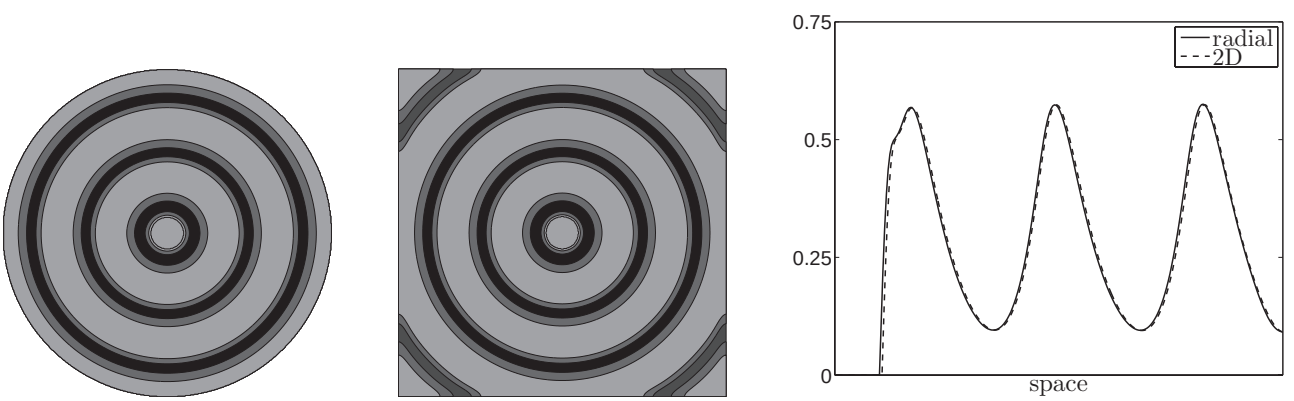

(a) (b) (c)

Fig. 15. Traveling wave solutions for predator with obstacle for (a) radially symmetric domain, (b) two-dimensional space and (c) comparison between radially symmetric and 2D.

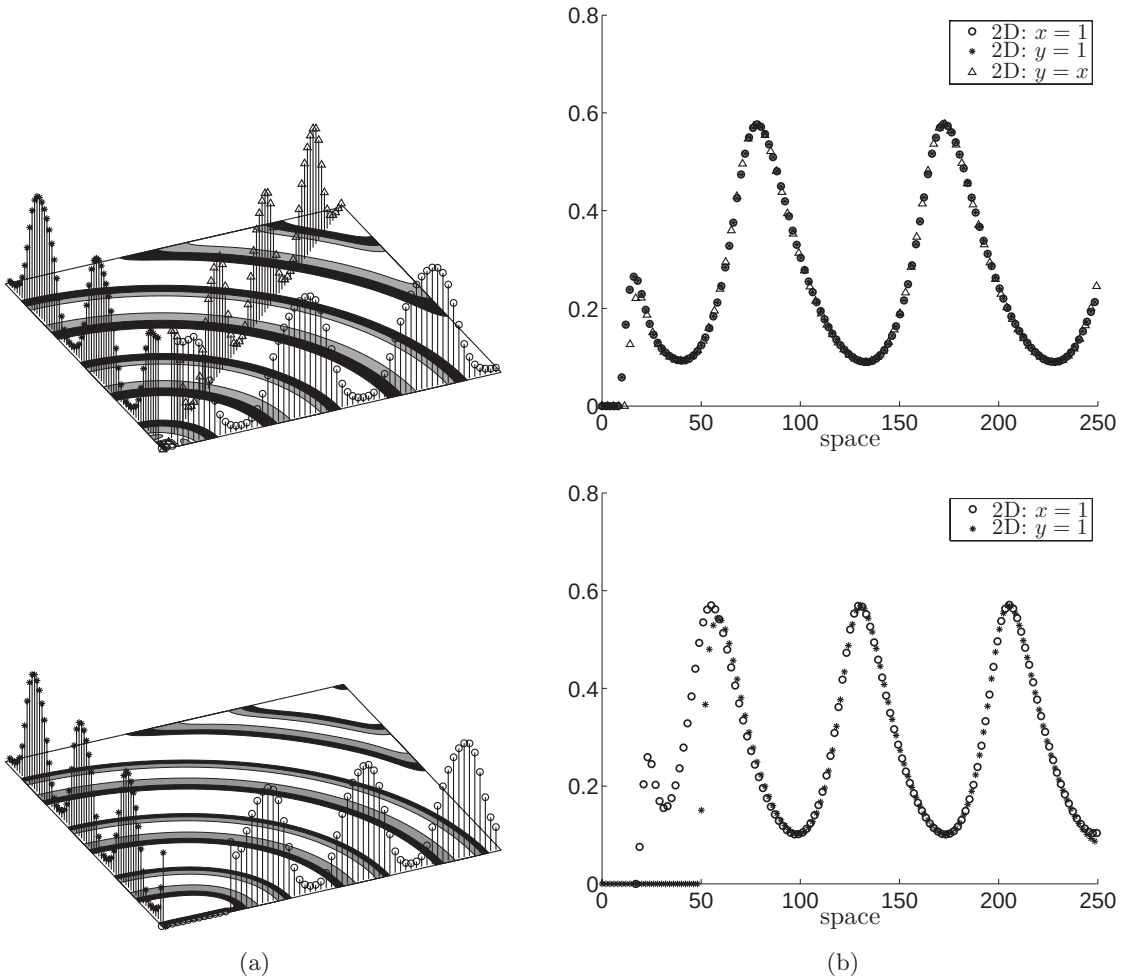

(a) (b)

Fig. 16. Predator solutions with obstacles $\Omega_o = (0, 10) \times (0, 10)$ (upper row) and $\Omega_o = (0, 50) \times (0, 2)$ (lower row). (a) The stem plot of $2D$ at $x = 1$, $y = 1$ and (b) overlapped spatial plots at $x = 1$, $y = 1$. For the upper rows, results for $y = x$ are included.

$r_b = m$, $m \in N$. And we define w_c and w_i as the radius of sectors of circumscribed and inscribed circles of the obstacle with origin as O, respectively. The obstacle domains are given as $\Omega^1_{o,k} = (0, 10) \times (0, k)$ for $k = 1, 2, \ldots, 10$. Table 3 shows the relationship between $\Omega_{o,k}$ and $w(n)$. Figure 17(a) shows the overlapped spatial plots for obstacle domains $\Omega^1_{o,1}$ (marked with circles) and the corresponding result from radially symmetric domain with $w(7)$ (marked with solid line). Likewise, Fig. 17(b) illustrates $\Omega^1_{o,10}$ (marked with circles) at $y = 1$ and corresponding $w(12)$ (marked with solid line), respectively. In this test, we shifted spatial plots and the results are completely matched. Figure 17(c) describes obstacle domains $\Omega^1_{o,1}$ (marked with circles) and $\Omega^1_{o,10}$ (marked with triangles) with w_c and w_i for $\Omega^1_{o,1}$ (marked with stars) and for $\Omega^1_{o,10}$ (dashed lines). As we have $w(7)$ and $w(12)$, we deduce that R lies between w_c and w_i.

Table 3. Comparison between rectangular obstacles and ω.

Case	Ω^1_{o1}	Ω^1_{o2}	Ω^1_{o4}	Ω^1_{o6}	Ω^1_{o8}	Ω^1_{o10}
w	$w(7)$	$w(8)$	$w(9)$	$w(10)$	$w(11)$	$w(12)$

For the second test, we investigate the circular obstacles with obstacle domains defined as $\Omega^2_{o,a,b}$ where a and b are one-half of the ellipse's major and minor axes. Table 4 shows the relationship between $\Omega^2_{o,10,b}$ and corresponding $w(n)$. Based on Table 4, corresponding values of $w(n)$ are $w(6)$ and $w(10)$, w lies between w_c and w_i.

Figure 18 shows temporal evolutions of the predator with triangle and rectangle shaped obstacles. The calculations are obtained for one-period

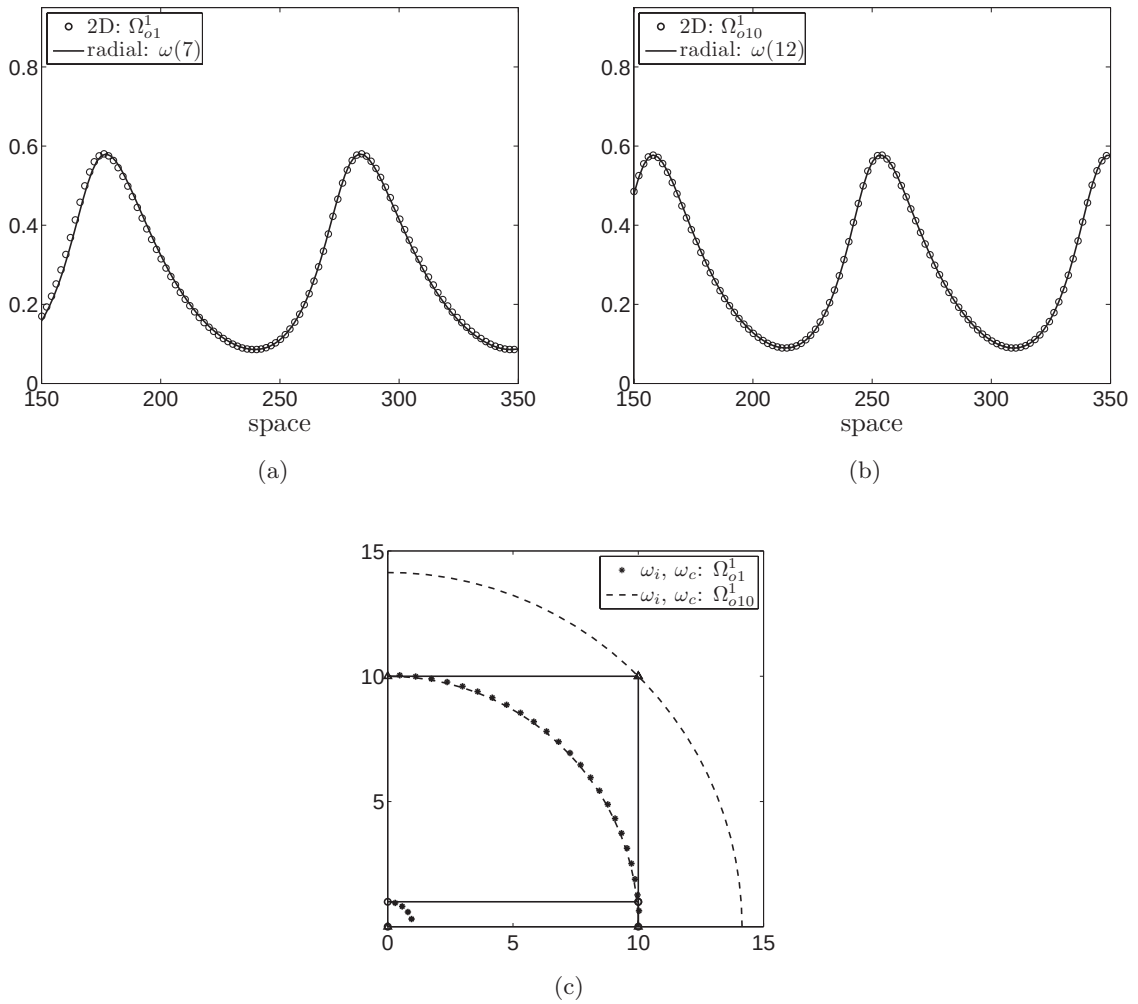

Fig. 17. (a) Overlapped spatial plots for $\Omega^1_{o,1}$ (marked with circles) at $y = 1$ corresponding to $w(7)$ (marked with solid line), (b) overlapped spatial plots for $\Omega^1_{o,10}$ (marked with circles) at $y = 1$ corresponding to $w(12)$ (marked with solid line) and (c) obstacle domains $\Omega^1_{o,1}$ (marked with circles) and $\Omega^1_{o,10}$ (marked with triangles) with w_c and w_i for $\Omega^1_{o,1}$ (marked with stars) and for Ω^1_{o10} (dashed lines), respectively.

at $t = 1500$, 1750, 2250, and 2750 (upper row) and $t = 1500$, 1625, 1750, and 1875 (lower row).

4.8. *Numerical experiments for formation of traveling wave solutions with nonconvex obstacle*

For the nonconvex obstacles, we observe the characteristics based on the wavelength as in the previous section. In $(0, 256) \times (0, 256)$, complex nonconvex obstacles with $\Omega^4_{o,1} = ((0, 5) \times (0, 10)) \cup ((0, 10) \times (0, 1))$ and $\Omega^4_{o,9} = ((0, 5) \times (0, 10)) \cup ((0, 10) \times (0, 9))$ are considered. Wavelengths are matched for $\Omega^4_{o,1}$ as $w(10)$ and $\Omega^4_{o,9}$ as $w(12)$. Figure 19(a) shows w_c and w_i for $\Omega^4_{o,1}$ (marked with circles) and $\Omega^4_{o,9}$. Circles and triangles depict the spatial plot at $x = 1$ and $y = 1$ for $\Omega^4_{o,9}$ with corresponding $w(10)$ (solid line) in Fig. 19(b). For the nonconvex obstacle, we have similar results as convex obstacles.

Table 4. Comparison between circular obstacles and ω.

Case	$\Omega^2_{o,10,2}$	$\Omega^2_{o,10,4}$	$\Omega^2_{o,10,6}$	$\Omega^2_{o,10,8}$	$\Omega^2_{o,10,10}$
w	$w(6)$	$w(7)$	$w(8)$	$w(9)$	$w(10)$

To observe more cases, Fig. 20 shows the nonconvex obstacles such as a polygon and a star with $w(10)$ and $w(12)$, respectively. The spatial plots for corresponding waves w are overlapped with (b) a polygon (dashed line) and (c) a star (dashed dots). We observe that the wavelengths are also between w_c and w_i.

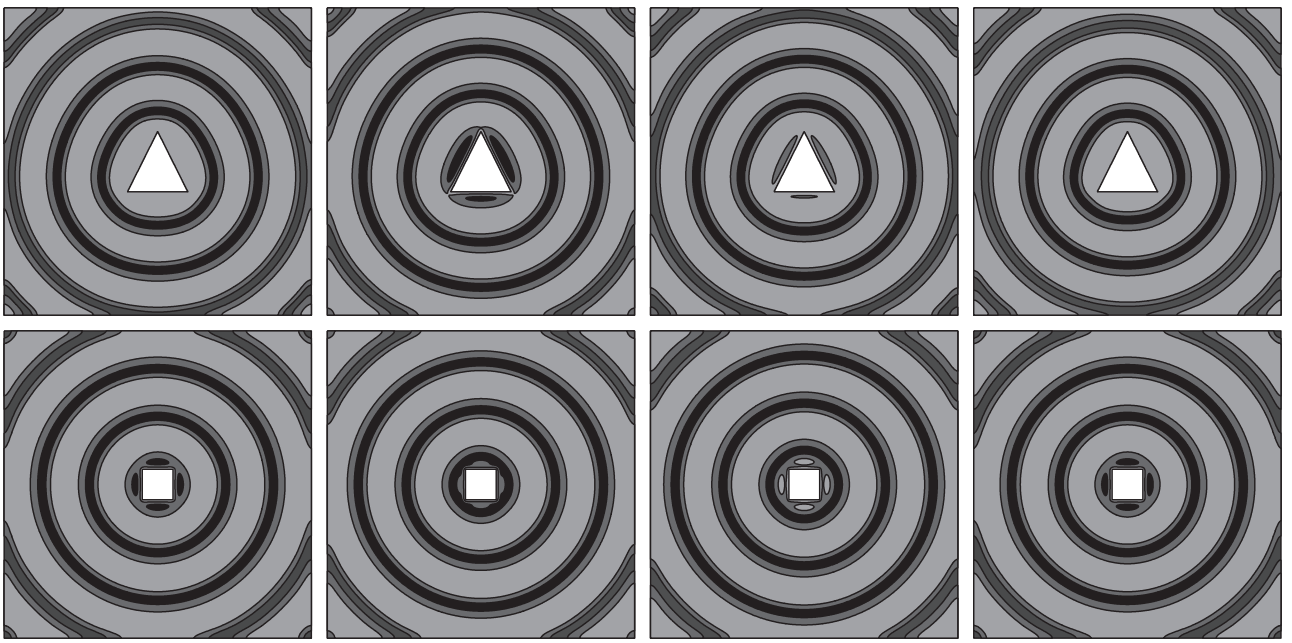

Fig. 18. Temporal evolutions of the predator with various convex obstacle domains. From left to right, $t = 1500$, 1750, 2250, and 2750 (upper row), $t = 1500$, 1625, 1750, and 1875 (lower row).

Figure 21 illustrates temporal evolutions for the predator with two shapes of obstacles. Compared to the nonconvex cases, the formation of the periodic traveling waves is different from the convex obstacles.

4.9. *Geometric landscape features*

In this section, we consider the traveling wave solutions around the geometric landscape features, which are obtained by using the image segmentation. The first geometric landscape is the large domain with an obstacle as the Kielder Water in northern Britain. Note that the regular periodic population dynamics for the predator is experimentally performed in [Lambin *et al.*, 1998]. Figures 22(a) and 22(b) show a whole view and a closed view of the predator at $t = 7000$. As can be seen that our numerical simulation indeed demonstrates the traveling wave solutions with complicated obstacles.

For the second example, the traveling wave solutions for the Inari region in Fennoscandia are considered. The population dynamics on islands in

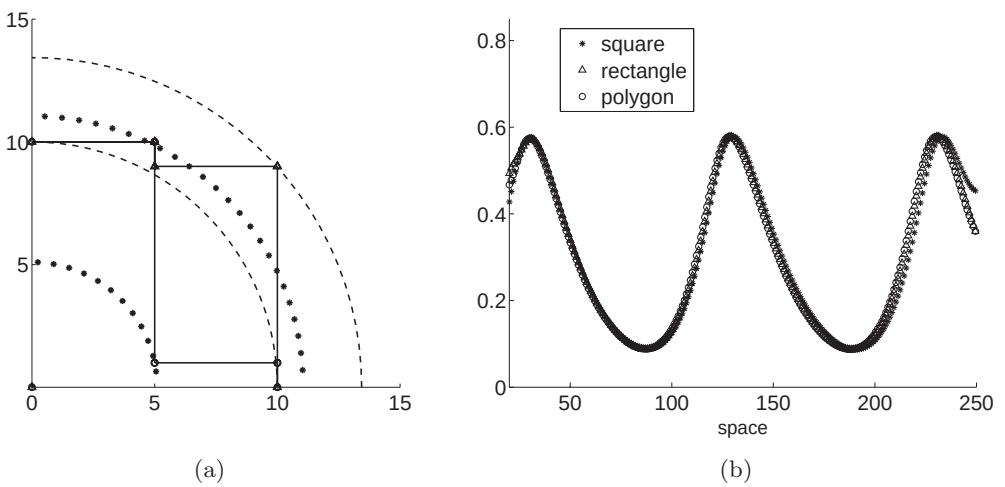

(a) (b)

Fig. 19. (a) Stars and dashed lines depict w_c and w_i for $\Omega^4_{o,1}$ (marked with circles) and $\Omega^4_{o,9}$ (marked with triangles) and (b) circles and triangles depict the spatial plot at $x = 1$ and $y = 1$ for $\Omega^4_{o,9}$ corresponding to $w(10)$ (solid line).

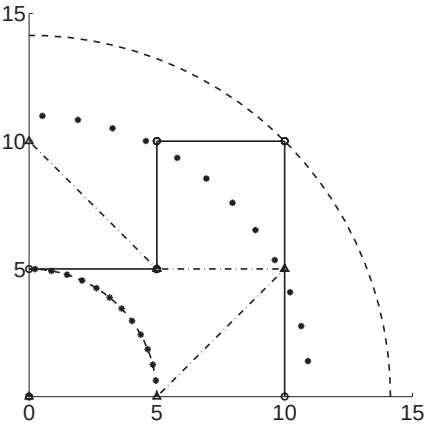

(a)

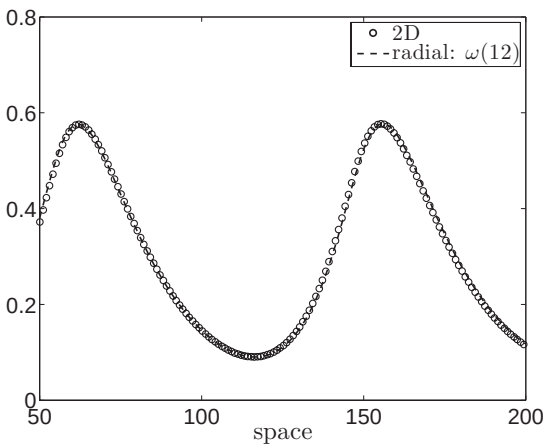

(b)

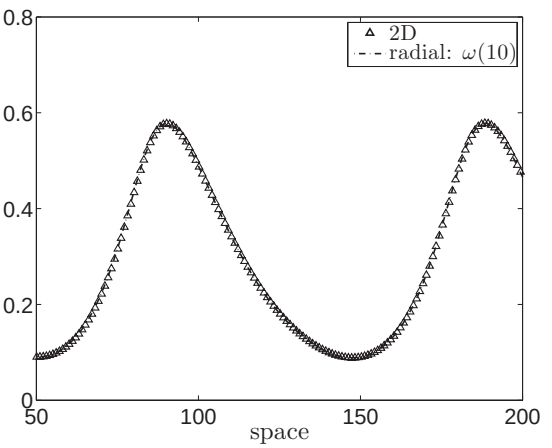

(c)

Fig. 20. (a) Stars and dots depict the range of R for a polygon (marked with circles) and a star (marked with triangles), (b) corresponding wavelengths with $w(10)$ (dashed line) and (c) corresponding wavelengths with $w(12)$ (marked with dashed dots).

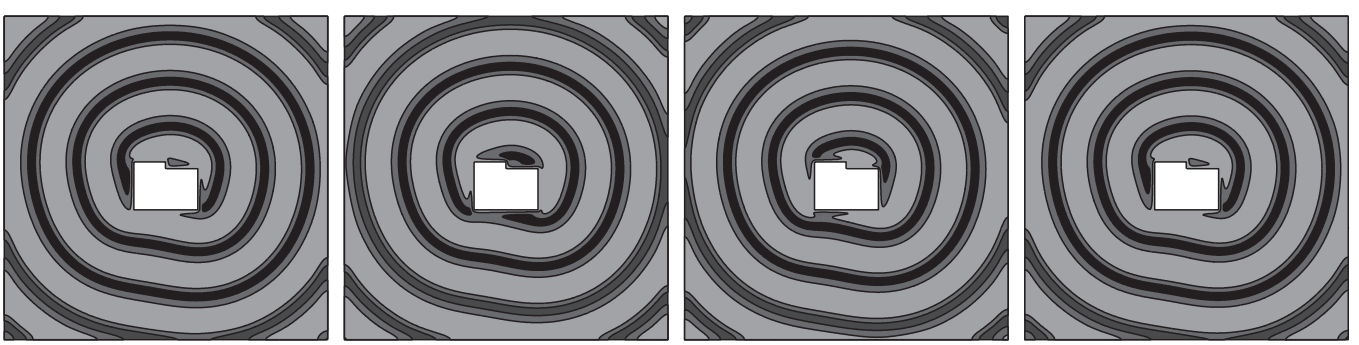

(a)

Fig. 21. Temporal evolution of the predator with various nonconvex obstacle domains. From left to right: (a) $t = 1625$, 1750, 1875, and 2125 and (b) $t = 2200$, 2800, 3400, and 3900.

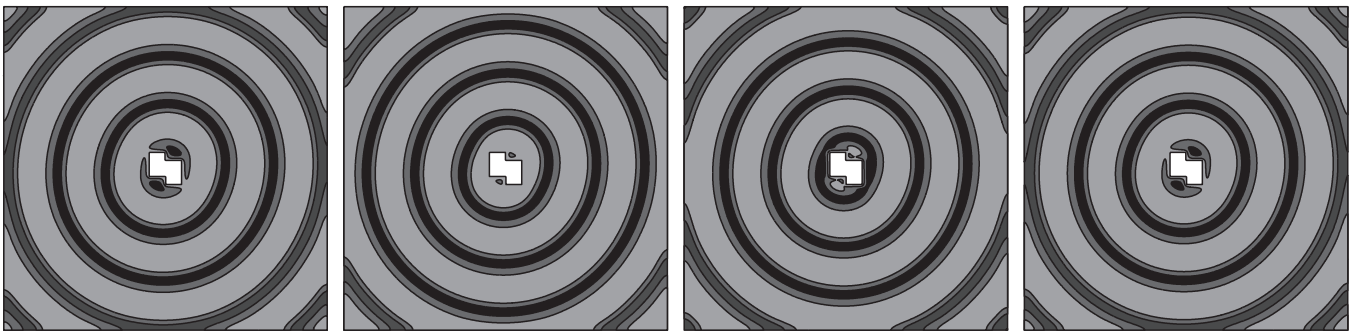

(b)

Fig. 21. (*Continued*)

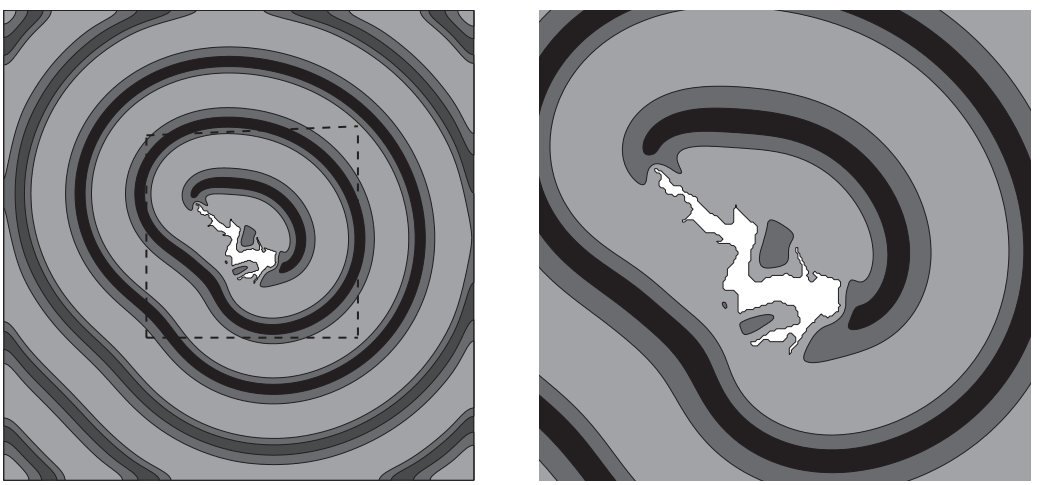

(a) (b)

Fig. 22. Traveling wave solutions with obstacle (Kielder Water) for the predator at: (a) $t = 7000$ and (b) closed up view of dashed region in (a).

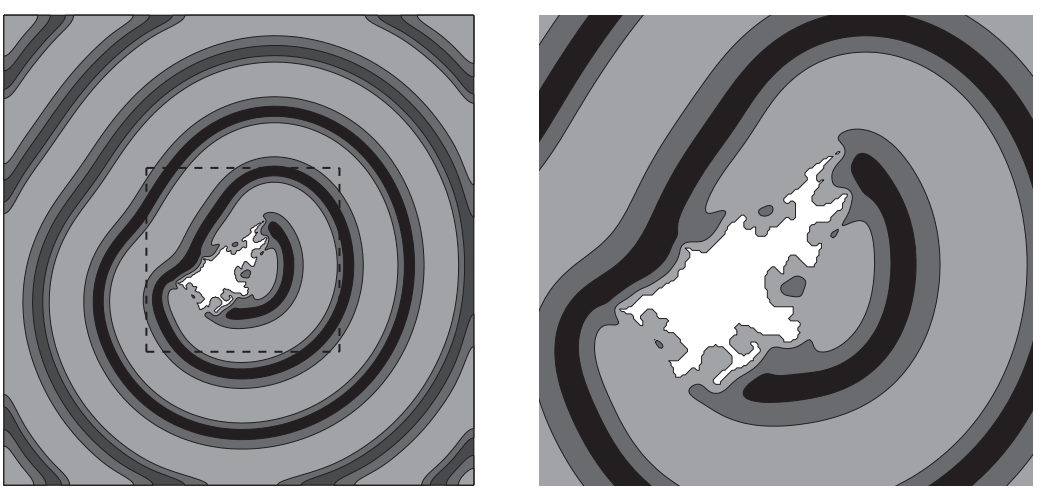

(a) (b)

Fig. 23. Traveling wave solutions having obstacle (the Lake Inari) for the predator at: (a) $t = 7000$ and (b) closed up view of dashed region in (a).

the Lake Inari for the regional synchrony was also experimentally studied by [Heikkilä *et al.*, 1994] in a small domain. The predator solution is illustrated in Fig. 23(a) at $t = 7000$. And a closed up view of dashed region in (a) is shown in Fig. 23(b). In a large domain, which has not been studied experimentally, numerical simulation can perform well to simulate the regular traveling wave.

5. Discussion

The periodic traveling wave solutions for the predator–prey model with landscape features have been studied after the work of Sherratt *et al.* [2002] who imposed homogeneous Dirichlet boundary at the edge of the obstacles. We have analyzed the numerical traveling wave solutions with robust and accurate numerical methods. For the regular periodic traveling wave solutions in spatiotemporal oscillations, we proposed a numerical algorithm for numerical periodicity to detect one-period of traveling wave solutions. Based on the assumption of the homogeneous Dirichlet boundary condition at the edge of the domain, we systematically investigate numerical solutions in one-, radially symmetric, and two-dimensional domains where the asynchrony behaviors are almost similar. Then we measured wavelengths to evaluate the spatial asynchrony around the two-dimensional obstacles, convex and nonconvex shapes where wavelengths are bounded. By adapting this method, we expect to have more general description for a generation of traveling wave solutions.

By the numerical simulations with realistic landscape features such as the Kielder Water and the Lake Inari, the generation of traveling wave solutions was able to be observed which takes a long time in field studies. Our investigation clearly reflected the regular periodicity and the geometric assumption with a larger domain including the Lake Inari suggesting movement of predator and prey. We expect that our numerical approach could give a good tool to investigate the ecological features, as well as provide a mathematical analysis.

Acknowledgments

The first author (A. Yun) acknowledges the support of the National Junior research fellowship from the National Research Foundation of Korea grant funded by the Korea government (No. 2011-00012258). The author (J. Shin) is supported by Basic Science Research Program through the National Research Foundation of Korea (NRF) funded by the Ministry of Education (2009-0093827). The corresponding author (J. S. Kim) was supported by the National Research Foundation of Korea (NRF) grant funded by the Korea government (MSIP) (NRF-2014R1A2A2A01003683). The authors are grateful to the reviewers whose valuable suggestions and comments significantly improved the quality of this paper.

References

Ascher, U., Ruuth, S. & Wetton, B. [1995] "Implicit-explicit methods for time-dependent partial differential equations," *SIAM J. Numer. Anal.* **32**, 797–823.

Banerjee, M. & Banerjee, S. [2012] "Turing instabilities and spatio-temporal chaos in ratio-dependent Holling–Tanner model," *Math. Biosci.* **236**, 74–76.

Benson, D. L., Sherratt, J. A. & Maini, P. K. [1993] "Diffusion driven instability in an inhomogeneous domain," *Bull. Math. Biol.* **55**, 365–384.

Borzi, A. [2004] "Solution of lambda–omega systems: Theta-schemes and multigrid methods," *Numer. Math.* **98**, 581–606.

Briggs, W. L. [1987] *A Multigrid Tutorial* (SIAM, Philadelphia).

Crooks, E. C. M., Dancer, E. N., Hilhorst, D., Mimura, M. & Ninomiya, H. [2004] "Spatial segregation limit of a competition-diffusion system with Dirichlet boundary conditions," *Nonlin. Anal.: Real World Appl.* **5**, 645–665.

Cross, M. C. & Hohenberg, P. C. [1993] "Pattern formation outside of equilibrium," *Rev. Mod. Phys.* **65**, 851.

Deng, S., Guo, B. & Wang, T. [2013] "Travelling wave solutions of the Green–Naghdi system," *Int. J. Bifurcation and Chaos* **23**, 1350087-1–8.

Dunbar, S. R. [1986] "Traveling waves in diffusive predator–prey equations: Periodic orbits and point-to-periodic heteroclinic orbits," *SIAM J. Appl. Math.* **46**, 1057–1078.

Garvie, M. R. [2007] "Finite-difference schemes for reaction–diffusion equations modeling predator–prey interactions in MATLAB," *Bull. Math. Biol.* **69**, 931–956.

Heikkilä, J., Below, A. & Hanski, I. [1994] "Synchronous dynamics of microtine rodent populations on islands in Lake Inari in northern Fennoscandia: Evidence for regulation by mustelid predators," *Oikos* **70**, 245–252.

Ims, R. A. & Andreassen, H. P. [2000] "Spatial synchronization of vole population dynamics by predatory birds," *Nature* **408**, 194–196.

Kopell, N. & Howard, L. N. [1973] "Plane wave solutions to reaction–diffusion equations," *Stud. Appl. Math.* **52**, 291–328.

Lambin, X., Elston, D. A., Petty, S. J. & MacKinnon, J. L. [1998] "Spatial asynchrony and periodic travelling waves in cyclic populations of field voles," *Proc. Roy. Soc. B* **265**, 1491–1496.

Li, J. & Qiao, Z. [2012] "Bifurcations and exact traveling wave solutions of the generalized two-component Camassa–Holm equation," *Int. J. Bifurcation and Chaos* **22**, 1250305-1–13.

Li, Y., Jeong, D., Shin, J. & Kim, J. S. [2013] "A conservative numerical method for the Cahn–Hilliard equation with Dirichlet boundary conditions in complex domains," *Comput. Math. Appl.* **65**, 102–115.

Lotka, A. J. [1925] *Elements of Physical Biology* (Williams and Wilkins, Baltimore).

Mackin-Rogalska, R. & Nabaglo, L. [1990] "Geographical variation in cyclic periodicity and synchrony in the common vole, Microtus arvalis," *Oikos* **59**, 343–348.

MacKinnon, J. L., Lambin, X., Elston, D. A., Thomas, C. J., Sherratt, T. N. & Petty, S. J. [2001] "Scale invariant spatio-temporal patterns of field vole density," *J. Anim. Ecol.* **70**, 101–111.

Myrberget, S. [1973] "Geographical synchronism of cycles of small rodents in Norway," *Oikos* **24**, 220–224.

Ranta, E. & Kaitala, V. [1997] "Travelling waves in vole population dynamics," *Nature* **390**, 456.

Ruuth, S. J. [1995] "Implicit–explicit methods for reaction–diffusion problems in pattern formation," *J. Math. Biol.* **34**, 148–176.

Sherratt, J. A., Lambin, X., Thomas, C. J. & Sherratt, T. N. [2002] "Generation of periodic waves by landscape features in cyclic predator–prey systems," *Proc. Roy. Soc. Lond. B* **269**, 327–334.

Sherratt, J. A. & Smith, M. J. [2008] "Periodic travelling waves in cyclic populations: Field studies and reaction–diffusion models," *J. Roy. Soc. Interf.* **5**, 483–505.

Smith, M. J., Sherratt, J. A. & Armstrong, N. J. [2008] "The effects of obstacle size on periodic travelling waves in oscillatory reaction–diffusion equations," *Proc. Roy. Soc. A* **464**, 365–390.

Steen, H., Ims, R. A. & Sonerud, G. A. [1996] "Spatial and temporal patterns of small-rodent population dynamics at a regional scale," *Ecology* **77**, 2365–2372.

Upadhyay, R. K., Kumari, N. & Rai, V. [2010] "Modeling spatiotemporal dynamics of vole populations in Europe and America," *Math. Biosci.* **223**, 47–57.

Volterra, V. [1926] "Fluctuations in the abundance of a species considered mathematically," *Nature* **118**, 558–560.

Waite, J. J., Virgin, L. N. & Wiebe, B. [2014] "Competing responses in a discrete mechanical system," *Int. J. Bifurcation and Chaos* **24**, 1430003-1–13.

Wang, H. [2012] "Dynamical behaviors and numerical simulation of a Lorenz-type system for the incompressible flow between two concentric rotating cylinders," *Int. J. Bifurcation and Chaos* **22**, 1250124-1–11.

Zhang, G., Jiang, D. & Cheng, S. S. [2007] "3-periodic traveling wave solutions for a dynamical coupled map lattice," *Nonlin. Dyn.* **50**, 235–247.

Zhong, X. [1996] "Additive semi-implicit Runge–Kutta methods for computing high-speed nonequilibrium reactive flows," *J. Comput. Phys.* **128**, 19–31.